

Effect of temperature and vapor-phase encapsulation on particle growth and morphology

Sheryl H. Ehrman,^{a)} Maria I. Aquino-Class, and Michael R. Zachariah
Chemical Science and Technology Laboratory, Building 221, Room B312, National Institute of Standards and Technology, Gaithersburg, Maryland 20899

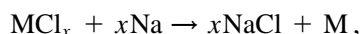
(Received 16 July 1998; accepted 27 October 1998)

The effect of *in situ* vapor phase salt-encapsulation on particle size and morphology was systematically investigated in a sodium co-flow/furnace reactor. The temperature of the furnace was varied, and the primary particle size and degree of agglomeration of the resulting silicon and germanium particles were determined from transmission electron micrograph images of particles sampled *in situ*. Particle size increased with increasing temperature, a trend expected from our understanding of particle formation in a high-temperature process in the absence of an encapsulant. Germanium, which coalesces faster than silicon, formed larger particles than silicon at the same temperatures, also in agreement with observations of particle growth in more traditional aerosol processes. At the highest temperatures, unagglomerated particles were formed, while at low temperatures, agglomerated particles were formed, with agglomerate shape following the shape of the salt coating.

I. INTRODUCTION

Combustion synthesis has been used to produce a variety of important aerosol materials such as carbon black, fumed silica, and titania paint pigments.¹ High product purity and ease of scale-up are some advantages of flame synthesis. However, the aerosol products are typically agglomerated, an undesirable characteristic if the materials are to be compacted following the aerosol processing step. Another disadvantage is that the oxidizing environment of the flame limits the range of materials which can be produced. Both of these difficulties can be alleviated by the use of a gas-phase encapsulation process.

A diffusion reactor based upon sodium metal/metal halide reaction chemistry has been developed for the production of nonoxide materials.²⁻⁴ In this system, the general chemistry can be described by the reaction



where M is the desired product (metal or nonmetal), and x is an integer. Thermodynamic calculations show that high yields are feasible if the reaction takes place at low temperatures, less than 1700 K.^{5,6} Because of the difference between the equilibrium vapor pressure of the desired product (metal or nonmetal) and the salt, the product typically condenses before the salt, forming the encapsulated morphology shown in Fig. 1. A variety of materials have been produced using this reactor configuration including metallic titanium, titanium diboride, and metallic iron,^{3,7} yet particle growth dynamics in this

reactor have not been systematically investigated. In this study, we investigate whether the trends known to hold for particle formation by gas-to-particle conversion in the absence of an encapsulant (condensing salt) also hold for this system.

During the formation of particles by gas-to-particle conversion, particle growth occurs by particle-particle collisions and subsequent coalescence.⁸⁻¹⁰ The two important time scales are the time between particle-particle collisions and the time required for the particles to coalesce.¹¹ This process is illustrated schematically in Fig. 2. If the rate of coalescence is sufficiently fast so that the particles can coalesce completely between collisions (collision-limited growth), then spherical unagglomerated particles will result. If the rate of coalescence is slow compared to the collision rate (coalescence-limited growth), then agglomerates will form. For the case of coalescence-limited growth, it is well known that higher reactor temperatures result in larger primary particles because the rate of coalescence increases with increasing temperature.^{9,12-16} It has also been shown experimentally that the material properties of the aerosol, particularly the temperature-dependent

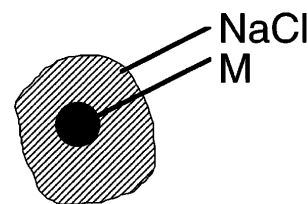


FIG. 1. Desired morphology for products of the salt-encapsulation process.

^{a)}Address all correspondence to this author. e-mail: ehrman@psi.ch

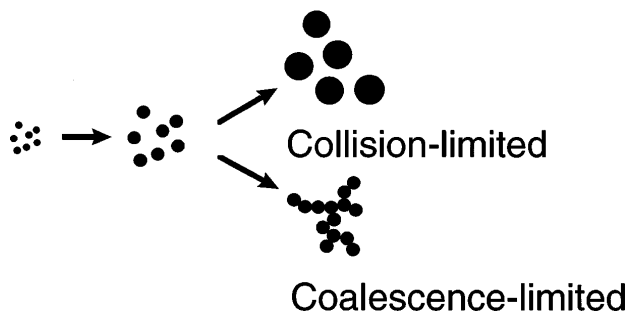


FIG. 2. Schematic showing unagglomerated particles resulting from collision-limited growth and agglomerates resulting from coalescence-limited aerosol growth.

coalescence rate, will have an effect on the morphology (particle size, degree of agglomeration) of the product. Materials which coalesce rapidly will form larger primary particles than materials which coalesce slowly, given the same time/temperature history.^{9,16–17}

Our objective is to investigate the effect of salt encapsulation on the morphology, as characterized by particle size and degree of agglomeration, of particles formed in a sodium co-flow/furnace reactor. In the experiments described here, salt-encapsulated particles of silicon and germanium are formed from their respective chloride precursors. These materials were chosen because they have similar valence and precursor chemistry, but differing behavior with respect to coalescence. The temperature of the furnace is varied, the speciation and phase of the materials present is determined using x-ray diffraction and Raman spectroscopy, and particle morphology is determined from transmission electron microscope images of the particles sampled *in situ*.

II. BACKGROUND

In order to test the effect of encapsulation and the material dependent coalescence rate, we needed to vary temperature over a wide range, while keeping the precursor decomposition chemistry constant. Silicon and germanium are similar in that they belong to the same chemical family (group IV semiconductors) and are available in identical form as precursors, SiCl_4 , and GeCl_4 ; however, they should have very different behaviors with respect to coalescence over the temperature range of the experiments. Silicon, with a melting temperature of 1683 K, is expected to sinter by solid state diffusion. It has been shown that the characteristic time for a particle undergoing coalescence via solid state diffusion is given by the equation¹⁸:

$$\tau = \frac{3 kT v_p}{64 \pi D \sigma v_o}, \quad (1)$$

where D , the diffusion coefficient, is represented by an equation of exponential form. v_p is the volume of the

particle undergoing coalescence, v_o the volume of the diffusing species, taken to be the atomic volume of silicon, and σ surface tension. This equation has recently been shown to predict the coalescence behavior of silicon clusters (<480 atoms) simulated using molecular dynamics calculations.¹⁹

Solid-state diffusion occurs predominantly via surface, volume, and grain boundary diffusion mechanisms. Theoretical calculations in the temperature range 1273 to 1573 K indicate that in the absence of a surface layer of oxide, surface diffusion is the dominant mechanism for the coalescence of silicon.²⁰ These results have been recently corroborated by molecular dynamics calculations.¹⁹ At 1273 K, the next most active mechanism is grain boundary diffusion, but its contribution is eight orders of magnitude less than that of surface diffusion. Because of the total dominance of the surface diffusion mechanism at 1273 K, it is assumed to also be the dominant mechanism at temperatures down to 1023 K, the lowest furnace temperature used in our experiments. A surface diffusion coefficient has been experimentally determined by Robertson²¹:

$$D = 9.36 \times 10^6 \exp\left(\frac{-298}{RT}\right) \quad (2)$$

with the units of D in $\text{cm}^2 \text{s}^{-1}$ and the activation energy in units of kJ mole^{-1} . Incorporating the surface diffusion coefficient and using a literature value for the surface tension²² gives the coalescence time as a function of temperature T , and initial particle diameter d_p , in cm:

$$\tau = 7.2 \times 10^{-8} d_p^3 T \exp\left(\frac{3.58 \times 10^4}{T}\right). \quad (3)$$

Germanium, with a melting temperature of 1210 K, is expected to coalesce by viscous flow at temperatures greater than the melting temperature, with the characteristic coalescence time given by²³

$$\tau = \frac{\eta d_p}{\sigma}. \quad (4)$$

Here, η is the viscosity of the material, reported as a function of temperature by Korunski and Bondareva.²⁴ Incorporating an exponential fit to the viscosity data, and a literature value for surface tension,²² the coalescence time as a function of temperature and initial particle diameter, in cm, is given by

$$\tau = 11 d_p \exp\left(\frac{2980}{T}\right). \quad (5)$$

For growth in regimes where coalescence is limiting, it has been proposed that particle growth rate is inversely proportional to the coalescence time.^{10,15} Without resorting to a detailed model of particle growth, we can look at the coalescence times of the two species

to predict relative particle size. Coalescence time as a function of inverse particle temperature, calculated for the coalescence of two particles, 50 nm in diameter, is shown for temperatures ranging from 1200 to 1400 K in Fig. 3. For both silicon and germanium, the coalescence time decreases with increasing temperature. For these materials, the surface diffusion coefficient of silicon is more temperature sensitive than either the viscosity of liquid germanium or the surface tension of either material. As a result, the coalescence time of silicon is much more temperature sensitive than the germanium coalescence time. For a single component system in the absence of an encapsulant, we expect both silicon and germanium to form larger primary particles at higher temperatures. In addition, since germanium coalesces much faster than silicon, especially at the lower range of temperatures used in these experiments, it is expected that the germanium primary particles should be larger than silicon primary particles formed at a given temperature. In the following experiments, we form silicon and germanium particles in the presence of an encapsulant to test if these hypotheses hold for a particle formation/encapsulation process.

III. EXPERIMENTAL PROCEDURES

A schematic of the cylindrical co-flow reactor is shown in Fig. 4. The flow rates used are given in Table I. All flows were controlled using calibrated mass flow controllers. The burner consists of three stainless steel concentric tubes and a central graphite injector with inside/outside diameters of 13/16, 25/32, and 95/102 mm for the stainless steel tubes and 3.2/9 mm for the graphite injector. The chloride precursors, SiCl_4 (99.9%), and GeCl_4 (99.9%), liquids with high vapor pressures at room temperature, were delivered to the burner by bubbling argon through the liquid precursors. The amount of precursor delivered to the burner

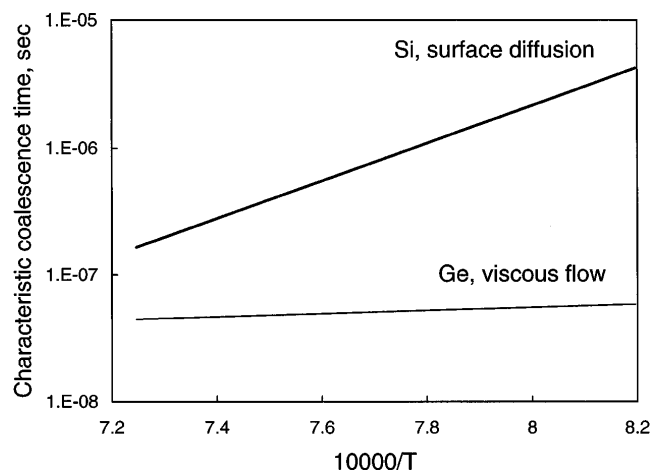


FIG. 3. Characteristic coalescence times calculated for silicon and germanium using Eqs. (3) and (5), respectively.

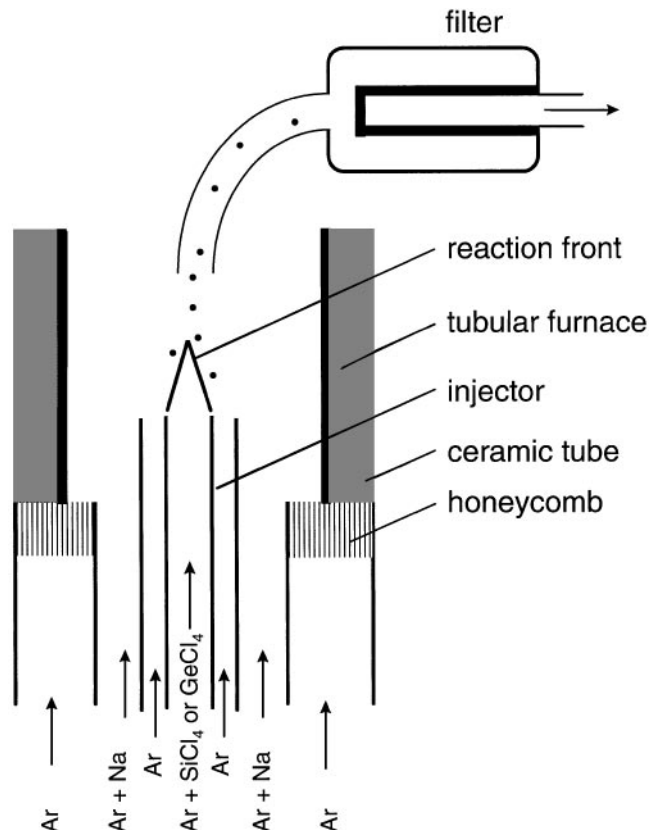


FIG. 4. A schematic of the cylindrical co-flow sodium reactor.

TABLE I. Flow rates used in sodium co-flow reactor.

Flow rates, 1 min^{-1} STP	Si experiments	Ge experiments
Ar flow through precursor bubbler	0.013	0.038
Diluent Ar	0.025	0.00
Ar inner shroud	0.15	0.15
Ar through sodium reservoir	1.5	1.5
Ar outer shroud	11.8	11.8

was estimated from the known vapor pressures of the precursors, assuming the vapor leaving the bubblers is saturated. The molar flow rate of each precursor was kept constant for each experiment at $2.6 \times 10^{-6} \text{ moles s}^{-1}$. The chloride precursors were introduced through the central graphite injector. Because the vapor pressure of GeCl_4 is less than that of SiCl_4 , diluent argon was added to the injector flow in the SiCl_4 experiments to keep the total injector flow rate constant. The next flow stream consists of argon, followed by sodium/argon, and an argon shroud gas in the outermost flow stream. The inner inert stream acts as a diffusion barrier to prevent particle formation and deposition at the burner mouth. The outer inert shroud acts to maintain a steady flow and an oxygen-free environment in the reaction zone. To ensure laminar flows, the sodium/argon annular channel was packed with a layer of steel wool, approximately

1 cm thick, and a stainless steel honeycomb was placed at the exit of the outer inert shroud.

The sodium was liquefied in a heated reservoir, maintained at a temperature of 900 K. Assuming the argon leaves the reservoir saturated with sodium, this corresponds to a sodium concentration in the argon stream of approximately 5 mol%, and a molar flow rate of sodium of 5.6×10^{-5} moles s^{-1} . With these flow rates, a closed-tip reaction front at the interface between the sodium and precursor flows was produced.

A platinum-wound alumina tube furnace, 11.4 cm in length, constructed in-house, rested on top of the outer inert shroud honeycomb, restricting the effective outer diameter to 5.1 cm. The temperature of the furnace was controlled via a thermocouple in contact with the outer wall of the furnace, approximately 6 cm from the base. The furnace temperature was varied from 1023 to 1373 K, and the residence time in the furnace zone ranged from approximately 0.5 s at 1023 K to 0.35 s at 1373 K. The entire outside of the burner, as well as the lines leading up to it, were wrapped in heating tape, covered with ceramic-fiber blanket insulation and maintained at a temperature of 973 K to prevent sodium from condensing in the lines.

Particles were collected using a 18 cm long, 0.6 cm inner diameter stainless-steel flexible tube positioned over the center of the burner, approximately 9 cm above the burner mouth. The particles were filtered onto a $10 \mu\text{m}$ pore size stainless-steel filter. At the end of each experiment, the particles were scraped from the filter, and the phases present were determined using x-ray diffraction (XRD) and Raman spectroscopy. The x-ray diffractometer used was a Philips 1830H. (Mention of brand names does not imply or constitute endorsement by NIST.) Raman scattering was excited in a backscattering geometry with an argon ion laser (Spectra Physics) operating at 514.5 nm, and a power density at the sample of less than 3 W cm^{-2} . The scattered radiation was collimated and focused onto the slits of a 0.46 M imaging spectrograph (ISA) which dispersed the radiation onto an 1100×330 pixel array, back illuminated, liquid-nitrogen cooled, charge coupled device camera system (Princeton Instruments). To collect particles for imaging using a Philips EM400 transmission electron microscope (TEM), a formvar-coated copper TEM grid was rapidly inserted into the center of the burner approximately 2.5 cm below the top of the furnace. The particles deposit onto the grid by thermophoresis.

IV. RESULTS AND DISCUSSION

A. Behavior of the encapsulant

Because the concentration of precursors in the reactor, and hence the concentration of chlorine, is the same for both silicon and germanium, the salt encapsulation

process is independent of the material. In the reaction zone, gas-phase sodium reacts with either SiCl_4 or GeCl_4 to form salt and silicon or germanium, all initially in the gas phase. The resulting supersaturation ratios of silicon and germanium at the reactor temperatures are extremely high, greater than 10^7 . A calculation of the critical nucleus diameter for both silicon and germanium at the highest furnace temperature, 1373 K, using classical nucleation theory gives a diameter much less than that of a silicon or germanium atom. This indicates that nucleation of silicon and germanium is not governed by an activated process at these temperatures, and as such, we expect silicon and germanium particles to form immediately downstream of the reaction zone with particle formation governed by kinetics of vapor-phase polymer formation.²⁵

The equilibrium vapor pressure of salt as a function of temperature is shown, along with the vapor pressure of salt in the reactor assuming complete reaction of the precursor species, as a function of temperature in Fig. 5. For heterogeneous condensation of either liquid-phase salt, at temperatures greater than its melting point of 1073 K, or solid-phase salt onto the germanium or silicon particles, the vapor pressure of salt in the reactor must be greater than the equilibrium vapor pressure at the reactor temperature.²⁶ From Fig. 5, it is apparent that this condition is met over the entire range of furnace temperatures in these experiments.

B. Particle morphology and structure

Transmission electron micrographs of the salt-encapsulated silicon and germanium particles formed at the highest furnace temperature, 1373 K, are shown in Fig. 6. The salt-coated particles are quite electron dense, preventing imaging of the silicon or germanium

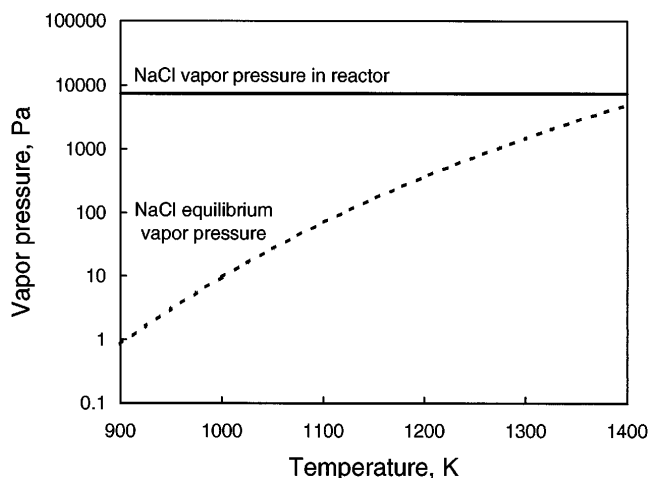


FIG. 5. Equilibrium vapor pressure of salt as a function of temperature. Solid line shows vapor pressure of salt in furnace region assuming complete reaction between precursor and salt.

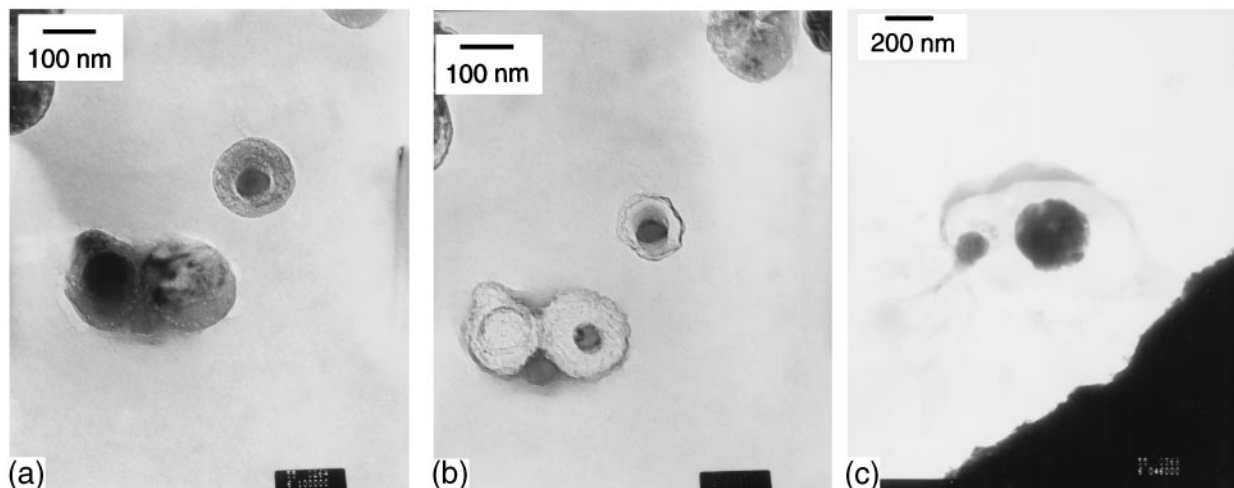


FIG. 6. Transmission electron microscope images of silicon and germanium particles formed at a furnace temperature of 1373 K: (a) coated silicon particles, (b) the same silicon particles shown in (a) with the salt coating removed, and (c) particles of germanium with the coating removed.

particles contained inside the salt. Fortunately, the electron beam can be used to vaporize the salt coating, allowing us to image both the as-coated silicon or germanium particles and the particles with the coating removed. A “before” image of coated silicon particles is shown in Fig. 6(a), and “after” images of silicon and germanium particles are shown in Figs. 6(b) and 6(c), respectively. Enrichment of either silicon or germanium in the dark regions was observed with energy dispersive x-ray analysis (EDS). In both cases, the silicon and germanium particles were unagglomerated, and no uncoated particles were observed. The most apparent difference between the two samples is the difference in size between the silicon and germanium particles. From measurements of 50 particle diameters, an approximate average diameter of 90 nm for silicon and 280 nm for germanium was observed, an expected result considering the characteristic coalescence times shown in Fig. 3.

To confirm the EDS results and to check for the presence of undesirable oxides, x-ray diffraction (XRD) patterns were obtained for each sample. The XRD patterns for silicon and germanium particles formed at 1373 K are shown in Figs. 7 and 8. The results for the lower temperature samples were similar. In the XRD pattern shown in Fig. 7, only peaks corresponding to silicon and salt were observed, indicating that the particles are not oxidized. In the XRD pattern for germanium, shown in Fig. 8, no peaks corresponding to germanium oxide, GeO_2 , were observed. Because of considerable overlap between the salt and germanium diffraction patterns, another technique, Raman spectroscopy, was used to confirm the presence of elemental germanium. The Raman spectrum obtained from a sample of germanium particles formed at 1373 K is shown in Fig. 9. The only significant feature in the spectrum, the peak at

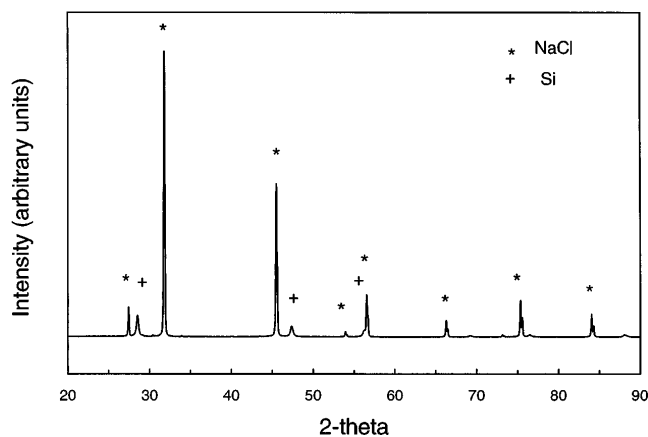


FIG. 7. X-ray diffraction pattern of salt-encapsulated silicon particles. The two phases present are metallic silicon and salt, indicating that the particles are not oxidized.

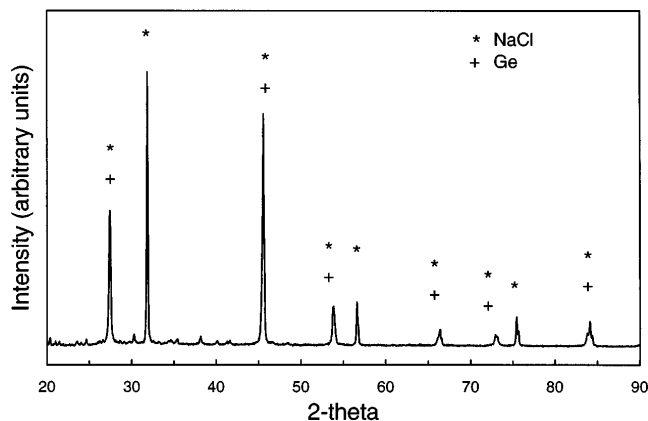


FIG. 8. X-ray diffraction pattern of salt-encapsulated germanium particles, showing the absence of any oxides.

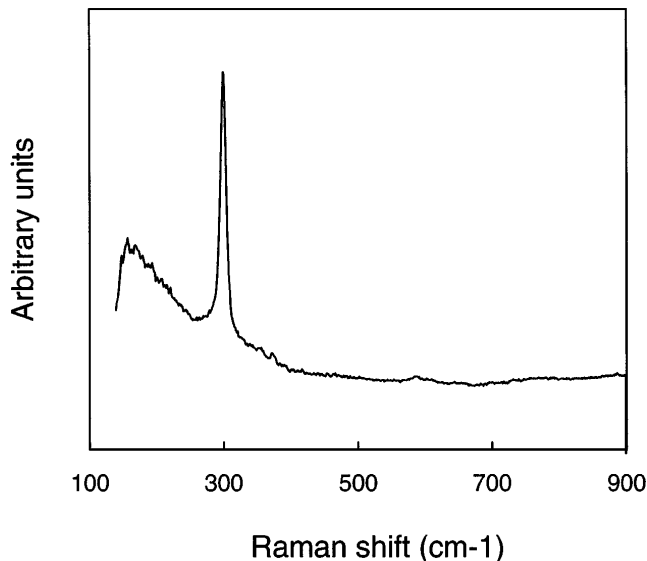


FIG. 9. Raman spectrum of salt-encapsulated germanium particles. Peak at $\sim 300 \text{ cm}^{-1}$ corresponds to the first-order transverse optical phonon mode of germanium.

$\sim 300 \text{ cm}^{-1}$, corresponds to the first-order transverse optical phonon mode of germanium.²⁷

From Fig. 3, as the temperature decreases, particle size should also decrease, a trend which was generally observed in our samples. In addition, we observed a transition from collision-controlled growth to coalescence-controlled growth with the onset of agglomeration occurring between 1323 and 1273 K for the silicon samples, and between 1273 and 1213 K for the germanium samples. TEM images of silicon and germanium agglomerates formed at an intermediate temperature of 1213 K are shown in Fig. 10. Because of the high density of the germanium agglomerates, it is difficult to discern individual primary particles. However, from measurements of distinct curved regions, we obtain a rough estimate of particle average diameter of 80 nm, and 60 nm for the silicon particles.

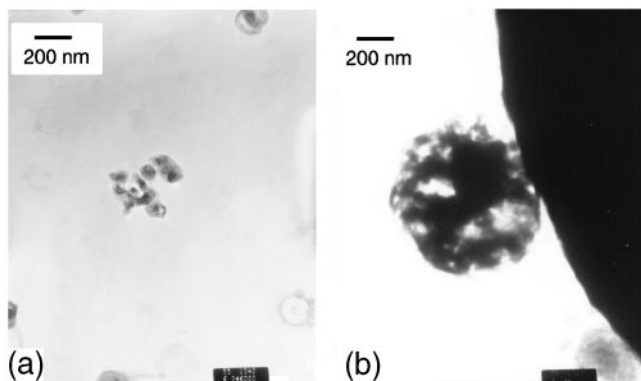


FIG. 10. Transmission electron microscope images of particles formed at 1213 K: (a) particles of silicon with the salt coating removed and (b) particles of germanium with the salt coating removed.

For both silicon and germanium, the agglomerates appeared to follow the shape of the salt coating. This is especially apparent in the 1023 K silicon sample, shown before the salt coating was removed in Fig. 11(a), and after in Fig. 11(b). In agglomerates formed in flames, the structures are typically more open, characterized by a fractal dimension of 1.5 to 1.9 or less.^{28–30} However, the surface tension of the salt acts to shape the agglomerates. Hence, an unintended consequence of this process may be the ability to vary the fractal dimension of the resulting structures from the low density structures characteristic of flame-generated aerosols to higher density structures with correspondingly higher specific surface area.

The appearance of agglomerated silicon particles at a furnace temperature of 1023 K, less than the melting temperature of salt (1074 K), was unexpected, as salt is expected to condense as a solid. However, the exothermicity of the reaction of sodium with SiCl_4 or GeCl_4 may also be a factor. Assuming that at the tip of the reaction front, the argon diluent layer has diffused away, and that the halide species is the limiting reagent, the adiabatic flame temperature is estimated to be 1430 K. If the furnace temperature is less than the melting temperature of salt, the heat released in the exothermic reaction zone may increase the temperature enough so that salt condenses as a liquid rather than as a solid, and therefore, agglomeration of the particles within the liquid salt droplets is possible.

A bimodal primary particle size distribution was also observed in the 1023 K silicon sample. As shown in Fig. 11, the agglomerates consisted of primary particles of either the larger size (60 to 100 nm) or of primary particles of the smaller size (20 to 40 nm). The flows in this reactor are laminar, and as discussed below, there is likely some degree of radial temperature variation in the reaction zone. The particles, formed immediately downstream of the reaction zone, should follow streamlines, agglomerating together with particles of the same temperature history (same size).

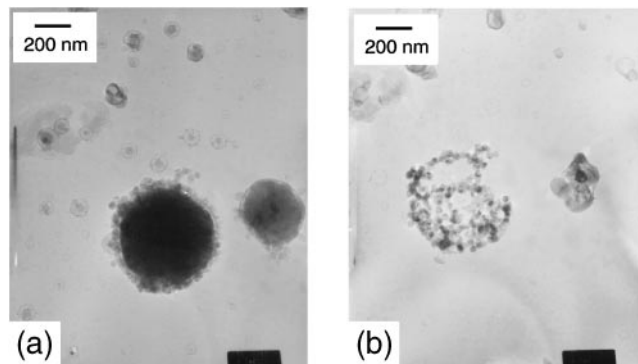


FIG. 11. Transmission electron microscope images of silicon particles formed at 1023 K: (a) salt-coated particles and (b) the same particles with the salt coating removed.

C. Sodium diffusion “flame”

The most significant difference between this reactor and a hydrocarbon diffusion flame is the nature of the chemistry at the reaction front. In the sodium reactor, the reactants are self-igniting, with no back diffusion of radical species required to propagate the flame. There is one important similarity: the shape and location of the reaction front adjusts so that at the reaction front, the concentrations of the reactants are in stoichiometric proportions. The inner coflow diluent stream in the sodium reactor provides a complication, however. In the absence of this layer, the temperature at any point on the reaction front should be constant. However, at the burner exit, the reacting species must diffuse through this layer of argon to react. It is expected that because of dilution, the temperature of the reaction front at the burner exit is lower than the temperature at the tip of the reaction front along the centerline.

D. Control of particle size and morphology

The variation of particle size with furnace temperature for all of the runs is shown for silicon in Fig. 12 and for germanium in Fig. 13. In both cases, particle size increases considerably for temperatures greater than 1213 K. As expected from Fig. 3, germanium particles are larger than silicon particles formed at each temperature. It is interesting to note that the germanium particle size changes considerably, yet the coalescence time of germanium is not a very strong function of temperature. In the presence of the encapsulant, condensation of the encapsulant and particle growth are occurring simultaneously. Particle growth is assumed to take place by collisions between encapsulated particles, followed by diffusion of the particles *within* the liquid salt droplet, with coalescence taking place as the particles

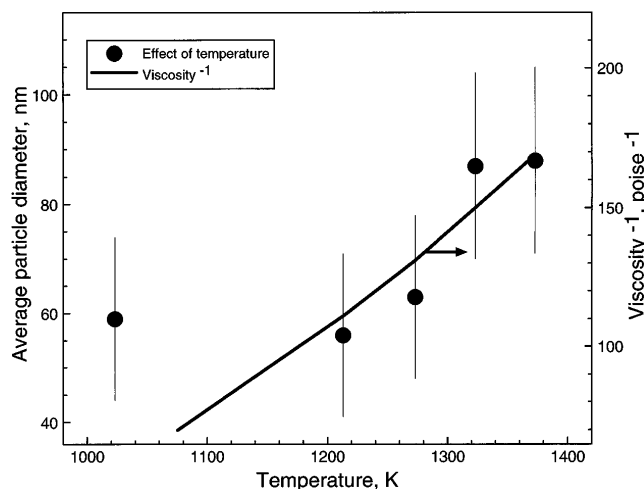


FIG. 12. Variation of particle size with furnace temperature for silicon. Vertical bar is equal to \pm the standard deviation of the particle size measurements.

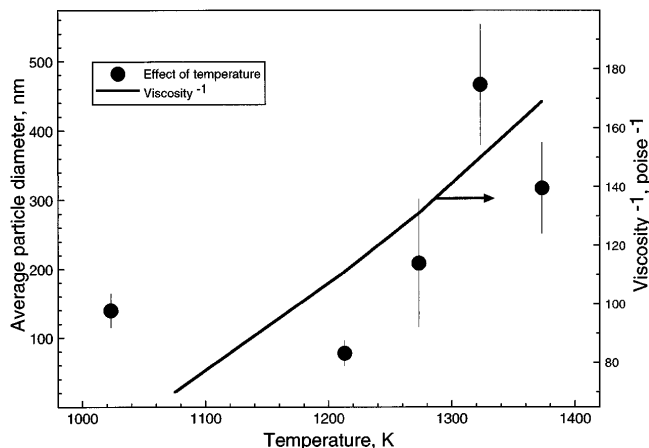


FIG. 13. Variation of particle size with furnace temperature for germanium. Vertical bar is equal to \pm the standard deviation of the particle size measurements.

come into contact with each other. The sensitivity of the germanium particle size to temperature may result in part because the primary particles must diffuse through the salt droplet before colliding with another particle. The presence of the salt encapsulant acts to decrease the rate of collisions between particles, thus reducing the particle size. According to the Stokes–Einstein relationship, the diffusivity of a particle in a continuum fluid (here, liquid salt) is inversely proportional to the viscosity of the liquid, which is shown for salt for temperatures greater than the melting temperature in Figs. 12 and 13. The agreement between the inverse of viscosity and the trend of increasing particle size with temperature, at the very least, suggests that the salt encapsulation is acting to control final particle size by impeding particle-particle interactions.

V. CONCLUSIONS

A systematic study of particle formation in a sodium co-flow reactor was conducted. The temperature of the furnace was varied, and the primary particle size of the resulting silicon and germanium particles was determined from TEM images of particles sampled *in situ*. In this system, the competing processes are the growth of the silicon and germanium particles and the condensation of the salt encapsulant. The following trends expected for particle formation by gas-to-particle conversion in the absence of an encapsulant were observed to hold for this system: (a) higher temperatures lead to larger particles, regardless of the material, and (b) materials which coalesce rapidly will form larger particles than materials which coalesce slowly. The presence of the salt may have affected the final primary particle size of both materials, as evidenced by the correlation between particle size and salt viscosity. This was especially apparent for germanium, which showed considerable

variation in particle size with respect to temperature, despite having the least temperature-sensitive coalescence rate. Salt-coated unagglomerated particles were observed at the highest temperature, 1373 K, and agglomerated particles were formed at lower temperatures, 1323 K for silicon and 1213 K for germanium. Interestingly, we observed that the agglomerates tended to follow the shape of the salt droplets leading to more dense (apparently higher fractal dimension) agglomerates than would be expected in the absence of salt.

ACKNOWLEDGMENT

The authors wish to thank Dr. James Maslar for performing the Raman spectroscopy measurements.

REFERENCES

1. G. D. Ulrich, Chemical and Engineering News, August 6 (1984).
2. R. L. Axelbaum, J. DuFaux, C. A. Frey, K. F. Kelton, S. A. Lawton, L. J. Rosen, and S. M. L. Sastry, *J. Mater. Res.* **11**, 948 (1996).
3. D. P. DuFaux and R. L. Axelbaum, *Comb. Flame* **100**, 350 (1995).
4. K. L. Steffens, M. R. Zachariah, D. P. DuFaux, and R. L. Axelbaum, *Chem. Mater.* **8**, 1871 (1996).
5. H. F. Calcote and W. Felder, *Twenty-Fourth Symposium (International) on Combustion* (The Combustion Institute, Pittsburgh, 1992), pp. 1869–1876.
6. I. Glassman, K. A. Davis, and K. Brezinski, *Twenty-Fourth Symposium (International) on Combustion* (The Combustion Institute, Pittsburgh, 1992), pp. 1877–1882.
7. N. Gorshkov, M. L. Aquino, R. D. Shull, A. Shapiro, and M. R. Zachariah, *Nanostruct. Mater.* (1997).
8. G. D. Ulrich and N. S. Subramanian, *Combustion Sci. Technol.* **17**, 119 (1977).
9. J. J. Helble and A. F. Sarofim, *J. Colloid Interface Sci.* **128**, 348 (1989).
10. W. Koch and S. K. Friedlander, *J. Colloid Interface Sci.* **140**, 419 (1991).
11. K. E. J. Lehtinen, R. S. Windeler, and S. K. Friedlander, *J. Aerosol Sci.* **27**, 883 (1996).
12. G. D. Ulrich, *Combust. Sci. Technol.* **4**, 47 (1971).
13. M. R. Zachariah and H. G. Semerjian, *High Temp. Sci.* **28**, 113 (1990).
14. M. K. Akhtar, Y. Xiong, and S. E. Pratsinis, *AIChE J.* **37**, 1561 (1991).
15. M. K. Wu, R. S. Windeler, C. K. R. Steiner, T. Boers, and S. K. Friedlander, *Aerosol Sci. Technol.* **19**, 527 (1993).
16. R. S. Windeler, K. E. J. Lehtinen, and S. K. Friedlander, *Aerosol Sci. Technol.* (1997).
17. Y. Xiong, M. K. Akhtar, and S. E. Pratsinis, *J. Aerosol Sci.* **24**, 301 (1993).
18. S. K. Friedlander and M. K. Wu, *Phys. Rev. B* **49**, 3622 (1994).
19. M. R. Zachariah and M. C. Carrier, *Science* (1997).
20. M. M. Lunden, Ph.D. Thesis, Department of Chemical Engineering, California Institute of Technology (1995).
21. W. M. Robertson, *J. Am. Ceram. Soc.* **64**, 9 (1981).
22. C. J. Smithells, *Smithells Metals Reference Book*, edited by E. A. Brandes and G. B. Brook, 7th ed. (Butterworth-Heinemann Ltd., 1992).
23. J. Frenkel, *J. Phys.* **9**, 385 (1945).
24. A. M. Korunski and A. G. Bondareva, *Russian J. Phys. Chem.* **47**, 1552 (1973).
25. M. R. Zachariah and W. Tsang, *Aerosol Sci. Technol.* **19**, 499 (1993).
26. W. C. Hinds, *Aerosol Technology* (Wiley-Interscience, New York, 1982).
27. F. Cerdiera, W. Dreybrodt, and M. Cardona, *Solid State Commun.* **10**, 591 (1972).
28. S. R. Forrest and T. A. Whitten, Jr., *J. Phys. A: Math. Gen.* **12**, 109 (1979).
29. R. J. Sampson, G. W. Mulholland, and J. W. Gentry, *Langmuir* **3**, 272 (1987).
30. D. W. Schaefer and A. J. Hurd, *Aerosol Sci. Technol.* **12**, 876 (1990).